Mechanism-based strain gradient plasticity—II. Analysis

Y. Huang [a,*], H. Gao [b], W.D. Nix [c], J.W. Hutchinson [d]

[a]*Department of Mechanical and Industrial Engineering, University of Illinois, Urbana, IL 61801, USA*
[b]*Division of Mechanics and Computation, Stanford University, Stanford, CA 94305, USA*
[c]*Department of Materials Science and Engineering, Stanford University, Stanford, CA 94305, USA*
[d]*Division of Engineering and Applied Sciences, Harvard University, Cambridge, MA 02138, USA*

Abstract

A mechanism-based theory of strain gradient (MSG) plasticity has been proposed in Part I of this paper. The theory is based on a multiscale framework linking the microscale notion of statistically stored and geometrically necessary dislocations to the mesoscale notion of plastic strain and strain gradient. This theory is motivated by our recent analysis of indentation experiments which strongly suggest a linear dependence of the square of plastic flow stress on strain gradient. Such a linear dependence is consistent with the Taylor plastic work hardening model relating the flow stress to dislocation density. This part of this paper provides a detailed analysis of the new theory, including equilibrium equations and boundary conditions, constitutive equations for the mechanism-based strain gradient plasticity, and kinematic relations among strains, strain gradients and displacements. The theory is used to investigate several phenomena that are influenced by plastic strain gradients. In bending of thin beams and torsion of thin wires, mechanism-based strain gradient plasticity gives a significant increase in scaled bending moment and scaled torque due to strain gradient effects. For the growth of microvoids and cavitation instabilities, however, it is found that strain gradients have little effect on micron-sized voids, but submicron-sized voids can have a larger resistance against void growth. Finally, it is shown from the study of bimaterials in shear that the mesoscale cell size has little effect on global physical quantities (e.g. applied stresses), but may affect the local deformation field significantly. © 1999 Elsevier Science Ltd. All rights reserved.

* Corresponding author. Tel.: +1-217-265-5072; fax: +1-217-244-6534.
  E-mail address: huang9@uiuc.edu (Y. Huang)

1. Summary of the mechanism-based strain gradient plasticity

Based on a multiscale framework linking the microscale notion of statistically stored and geometrically necessary dislocations to the mesoscale notion of plastic strain and strain gradient, we have derived the constitutive equations of the mechanism-based strain gradient (MSG) plasticity in Part I of this paper (Gao et al., 1999). The MSG plasticity constitutive equations, as well as equilibrium equations and kinematic relations among strains, strain gradients and displacements are summarized in this section to constitute a complete set of governing equations for mechanism-based strain gradient plasticity. We use MSG plasticity to investigate several phenomena that are influenced by plastic strain gradients, including bending of thin beams, torsion of thin wires, growth of microvoids, cavitation instabilities, and bimaterials in shear.

The deformation theory of the mechanism-based strain gradient plasticity is summarized in this section, while the MSG flow theory will be published elsewhere. For simplicity, elastic deformation and compressibility of materials are ignored in this paper. In addition, the theory and analysis are restricted to small deformation only.

1.1. Generalized stresses and strains in a strain gradient theory

Both strains and strain gradients are introduced in higher-order continuum theories of elasticity (Toupin, 1962; Koiter, 1964; Mindlin, 1964, 1965) and plasticity (Fleck and Hutchinson, 1993, 1997; Fleck et al., 1994; Gao et al., 1999). In a Cartesian reference frame x_i, the strain tensor ϵ_{ij} and strain gradient tensor η_{ijk} are related to the displacement u_i by (Fleck and Hutchinson, 1997)

$$\epsilon_{ij} = \frac{1}{2}(u_{i,j} + u_{j,i}) \tag{1}$$

and

$$\eta_{ijk} = u_{k,ij}, \tag{2}$$

which have the symmetry $\epsilon_{ij} = \epsilon_{ji}$ and $\eta_{ijk} = \eta_{jik}$. The condition of incompressibility can be stated as

$$\epsilon_{ii} = 0, \quad \eta_{ijk}^{\mathrm{H}} = \frac{1}{4}(\delta_{ik}\eta_{jpp} + \delta_{jk}\eta_{ipp}) = 0, \tag{3}$$

where η_{ijk}^{H} is the hydrostatic part of η_{ijk}, following the notation of Fleck and Hutchinson (1997).

The work increment per unit volume of an incompressible solid due to a variation of displacement δu_i is (Fleck and Hutchinson, 1997)

$$\delta w = \sigma_{ij}\delta\epsilon_{ij} + \tau_{ijk}\delta\eta_{ijk} = \sigma'_{ij}\delta\epsilon_{ij} + \tau'_{ijk}\delta\eta_{ijk}, \tag{4}$$

where the symmetric Cauchy stress σ_{ij} is the work conjugate of the variation of strain $\delta\epsilon_{ij}$; $\sigma'_{ij} = \sigma_{ij} - \sigma_{kk}\delta_{ij}/3$ is the deviatoric part of Cauchy stress; the symmetric higher-order stress τ_{ijk} ($\tau_{ijk} = \tau_{jik}$) is the work conjugate of the variation of strain gradient $\delta\eta_{ijk}$; and τ'_{ijk} is the deviatoric part of higher-order stress given by

$$\tau'_{ijk} = \tau_{ijk} - \frac{1}{4}(\delta_{ik}\tau_{jpp} + \delta_{jk}\tau_{ipp}) \tag{5}$$

such that $\tau'_{ipp} = 0$.

1.2. Equilibrium equations

Based on the principle of virtual work, Fleck and Hutchinson (1997) have shown that equilibrium equations for an incompressible solid can be written as

$$\sigma'_{ik,i} - \tau'_{ijk,ij} + H_{,k} + f_k = 0, \tag{6}$$

where f_k is the body force and H is a combined measure of the hydrostatic stress and higher-order stress according to

$$H = \frac{1}{3}\sigma_{kk} - \frac{1}{2}\tau_{jkk,j}. \tag{7}$$

For an incompressible solid, the double-stress tractions $\hat{r}_k$ tangential to the surface of the body are

$$\hat{r}_k = n_i n_j \tau'_{ijk} - n_k n_i n_j n_p \tau'_{ijp}. \tag{8}$$

The stress tractions $\hat{t}_k$ on the surface of the body are

$$\hat{t}_k = H n_k + n_i(\sigma'_{ik} - \tau'_{ijk,j}) + D_k(n_i n_j n_p \tau'_{ijp}) - D_j(n_i \tau'_{ijk}) + (n_i n_j \tau'_{ijk}$$
$$- n_k n_i n_j n_p \tau'_{ijp})(D_q n_q), \tag{9}$$

where n_i is the unit normal to the surface and D_j is the surface-gradient operator given by

$$D_j = (\delta_{jk} - n_j n_k)\frac{\partial}{\partial x_k}. \tag{10}$$

On the surface of the body, the gradient $\partial/\partial x_j$ can be resolved into the above surface gradient D_j and a normal gradient $n_j D$, i.e.

$$\frac{\partial}{\partial x_j} = D_j + n_j D, \tag{11}$$

where

$$D = n_k \frac{\partial}{\partial x_k}. \tag{12}$$

For the special case where the surface of the body has edges, there is a line traction $\hat{p}_k$ that must be taken into account (Fleck and Hutchinson, 1997). Suppose the surface has an edge C, formed by the intersection of two smooth surface segments $S^{(1)}$ and $S^{(2)}$. The unit normal to segment $S^{(i)}$ ($i = 1, 2$) is designated $n^{(i)}$, while the unit tangent $c^{(i)}$ along the edge C is defined with segment $S^{(i)}$ to the left. The line traction $\hat{p}_k$ is

$$\hat{p}_k = \Sigma(n_i k_j \tau'_{ijk} - k_k n_i n_j n_p \tau'_{ijp}), \tag{13}$$

where the summation is over both surfaces $S^{(1)}$ and $S^{(2)}$ at the edge C, and $k^{(i)}$ ($i = 1, 2$) is the unit outward normal to C lying within the surface $S^{(i)}$ given by $k^{(i)} = c^{(i)} \times n^{(i)}$ ($i = 1, 2$). (It should be pointed out that (13) corrects the misprint in Fleck and Hutchinson's (1997) expression for the line traction $\hat{p}_k$.)

1.3. Constitutive equations of MSG plasticity

The uniaxial stress–strain relation can be written, in general,

$$\sigma = \sigma_Y f(\epsilon), \tag{14}$$

where σ_Y is a measure of yield stress in uniaxial tension and f is a function of strain. For most ductile materials, the function f can be written as a power law relation,

$$f(\epsilon) = \left(\frac{E\epsilon}{\sigma_Y}\right)^N. \tag{15}$$

Here E is the Young's modulus and N is the plastic work hardening exponent ($0 \leq N < 1$). The flow stress σ, after incorporating the strain gradient effects, is (Nix and Gao, 1998; Gao et al., 1999)

$$\sigma = \sigma_Y \sqrt{f^2(\epsilon) + l\eta}, \tag{16}$$

where ϵ and η are the effective strain and effective strain gradient (Gao et al., 1999),

$$\epsilon = \sqrt{\frac{2}{3}\epsilon_{ij}\epsilon_{ij}}, \quad \eta = \frac{1}{2}\sqrt{\eta_{ijk}\eta_{ijk}}. \tag{17}$$

The characteristic material length l for strain gradient plasticity in (16) is given in

terms of the shear modulus μ and Burgers vector b by

$$l = 3\left(\frac{\alpha\mu}{\sigma_Y}\right)^2 b, \tag{18}$$

where α is an empirical material constant in Taylor's dislocation model for plastic work hardening of ductile materials, ranging from 0.2 to 0.5. For a typical ratio of shear modulus to yield stress, $\mu/\sigma_Y = 200$, and coefficient $\alpha = 0.4$, the characteristic material length l is 19,200 times the Burgers vector b. For copper ($b = 0.255$ nm), l is approximately 5 μ. For most engineering materials, the intrinsic material length l at which strain gradient effects are important is on the order of microns.

The constitutive equations for mechanism-based strain gradient plasticity are (Gao et al., 1999)

$$\sigma_{ij}' = \frac{2\epsilon_{ij}}{3\epsilon}\sigma, \tag{19}$$

$$\tau_{ijk}' = l_\epsilon^2\left[\frac{\sigma}{\epsilon}(\Lambda_{ijk} - \Pi_{ijk}) + \frac{\sigma_Y^2 f(\epsilon)f'(\epsilon)}{\sigma}\Pi_{ijk}\right], \tag{20}$$

where the flow stress σ is given in terms of the effective strain ϵ and effective strain gradient η in (16), and Λ_{ijk} and Π_{ijk} are given by

$$\Lambda_{ijk} = \frac{1}{72}\left[2\eta_{ijk} + \eta_{kij} + \eta_{kji} - \frac{1}{4}(\delta_{ik}\eta_{ppj} + \delta_{jk}\eta_{ppi})\right], \tag{21}$$

$$\Pi_{ijk} = \frac{1}{54}\frac{\epsilon_{mn}}{\epsilon^2}\left[\epsilon_{ik}\eta_{jmn} + \epsilon_{jk}\eta_{imn} - \frac{1}{4}(\delta_{ik}\epsilon_{jp} + \delta_{jk}\epsilon_{ip})\eta_{pmn}\right]. \tag{22}$$

The length l_ϵ in (20), as discussed in Part I of this paper (Gao et al., 1999), is the mesoscale cell size and is on the order of dislocation spacing at plastic yielding, L_{yield}, i.e.

$$l_\epsilon = \beta L_{\text{yield}} = \beta\frac{\mu}{\sigma_Y}b, \tag{23}$$

where $L_{\text{yield}} = \mu b/\sigma_Y$ is the mean spacing between statistically stored dislocations at plastic yielding, and β is a constant coefficient to be determined from experiments. In order to ensure that there are multiple dislocations within the mesoscale cell, it is suggested in Part I of this paper (Gao et al., 1999) that $\beta \geq 1$. On the other hand, in order to ensure that there are at least a few mesoscale cells within the characteristic material length l for strain gradient plasticity such that the homogenization at the mesoscale still holds in this multiscale framework, the cell size as well as the coefficient β cannot be too large. For typical metallic materials, the intrinsic material length l is on the order of 100 times the mean dislocation

spacing L_{yield} at plastic yielding (Gao et al., 1999). Therefore we suggest that β is between 1 and 10.

Eqs. (1), (2), (6), (19) and (20) constitute the governing equations for mechanism-based strain gradient plasticity. The traction boundary conditions are given in (8), (9) and (13). There are two constants in MSG plasticity that are to be determined by experiments, namely the coefficient α in Taylor's dislocation model for plastic work hardening and the normalized mesoscale cell size β in (23), ranging from 0.2 to 0.5 and from 1 to 10, respectively.

We use the mechanism-based strain gradient (MSG) plasticity theory to investigate several phenomena that are influenced by plastic strain gradient effects in the following sections, including bending of thin beams, torsion of thin wires, growth of spherical and cylindrical voids, cavitation instabilities, a bimaterial interface in shear and a fiber embedded in an infinite matrix in shear.

2. Bending of thin beams

In bending of ultra thin nickel beams with the beam thickness ranging from 12.5 to 100 μ, Stolken and Evans (1998) observed a strong size effect whereby thin beams (e.g. 12.5 μ thickness) display much stronger plastic work hardening than thick ones (e.g. 100 μ thickness). This size effect in bending cannot be explained by classical plasticity, which does not depend on an intrinsic material length. In this section, we use MSG plasticity to investigate bending of ultra-thin beams. For simplicity, we assume the beam is under plane-strain bending.

The Cartesian reference frame is set such that the x_1 axis coincides with the neutral axis of the beam, and bending is applied in the (x_1, x_2) plane. A unit beam width is taken in the out-of-plane (x_3) direction. The curvature is designated κ and the beam thickness is designated h. Strains in the Cartesian reference frame and the effective strain ϵ are given by

$$\epsilon_{11} = -\epsilon_{22} = \kappa x_2, \quad \epsilon_{12} = 0, \quad \epsilon = \frac{2}{\sqrt{3}} \kappa \, | \, x_2 \, |, \tag{24}$$

where ϵ_{22} is obtained from the assumptions of plane strain deformation $(\epsilon_{33} = 0)$ and incompressibility $(\epsilon_{kk} = 0)$. The corresponding displacement field is $u_1 = \kappa x_1 x_2, u_2 = -\frac{1}{2}\kappa(x_1^2 + x_2^2)$. The non-vanishing strain gradients in the Cartesian reference frame and the effective strain gradient η are given by

$$\eta_{112} = \eta_{222} = -\kappa, \quad \eta_{121} = \eta_{211} = \kappa, \quad \eta = \kappa. \tag{25}$$

The constitutive Eqs. (19) and (20) give non-vanishing deviatoric stresses and higher-order stresses as

$$\sigma'_{11} = -2\sigma'_{22} = \text{sign}(x_2)\frac{\sigma}{\sqrt{3}}, \tag{26}$$

$$\frac{6}{5}\tau'_{121} = \frac{6}{5}\tau'_{211} = -\tau'_{222} = 6\tau'_{233} = 6\tau'_{323} = \frac{\kappa l_\epsilon^2 \sigma_Y^2 f(\epsilon) f'(\epsilon)}{24\sigma}, \tag{27}$$

where sign(x_2) stands for the sign of x_2, σ is the flow stress given in (16), and l_ϵ is the mesoscale cell size in (23).

The equilibrium Eq. (6) and traction-free boundary conditions on the top and bottom surfaces of the beam ($x_2 = \pm h/2$) give the hydrostatic stress

$$H = -\sigma'_{22} + \frac{d\tau'_{222}}{dx_2}. \tag{28}$$

The double-stress traction $\hat{r}_k$ at the cross section of the beam is zero, while the non-vanishing stress traction is

$$\hat{t}_1 = H + \sigma'_{11} - 2\frac{d\tau'_{211}}{dx_2}.$$

There is a line traction at the edge between the cross section and top surface ($x_2 = h/2$) of the beam, given by $\hat{p}_1 = (2\tau'_{211} - \tau'_{222})_{x_2} = h/2$. The line traction at the edge between the cross section and bottom surface ($x_2 = -h/2$) is just the negative of the above expression. These stress and line tractions give a pure bending
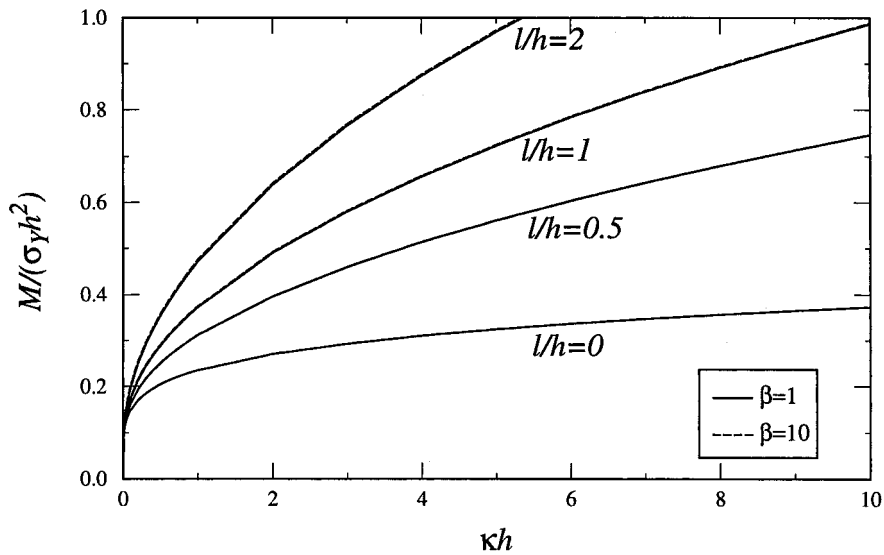

Fig. 1. The normalized bending moment, $M/(\sigma_Y h^2)$, vs the normalized curvature, κh, for several ratios of intrinsic material length to beam thickness, l/h, where σ_Y is the yield stress, h is the beam thickness, and l is the intrinsic material length for mechanism-based strain gradient plasticity. The limit $l/h = 0$ corresponds to classical plasticity. Plastic work hardening exponent $N = 0.2$, shear modulus $\mu = 200\sigma_Y$, the coefficient α for Taylor's dislocation model $= 0.4$, and the ratio β of mesoscale cell size l_ϵ to dislocation spacing at plastic yielding is 1 for solid lines and 10 for dashed lines.

moment M, i.e. there are no net forces or torques in the cross section. The bending moment M can be obtained from the integration over the cross section of moments induced by these tractions as

$$M = \int_{-h/2}^{h/2} \left[\frac{2}{\sqrt{3}} \mid x_2 \mid \sigma + \frac{\kappa l_\epsilon^2}{9} \frac{\sigma_Y^2 f(\epsilon) f'(\epsilon)}{\sigma} \right] dx_2. \tag{29}$$

This moment-curvature relation can also be obtained from the principle of virtual work by enforcing the equality of interval virtual work done by stresses and higher-order stresses in the beam and external virtual work done by the moment, similar to the method used by Fleck and Hutchinson (1997) for torsion.

The normalized bending moment, $M/(\sigma_Y h^2)$, vs the normalized curvature, κh, is shown in Fig. 1 for several ratios of intrinsic material length to beam thickness, l/h. The limit $l/h = 0$ corresponds to classical plasticity. The plastic work hardening exponent N is 0.2, the shear modulus μ is 200 times the yield stress σ_Y, and the coefficient α in (18) for Taylor's dislocation model is 0.4. These constants are also used in all of the following examples, except where explicitly noted otherwise. In order to investigate the sensitivity to the mesoscale cell size, l_ϵ, two ratios of cell
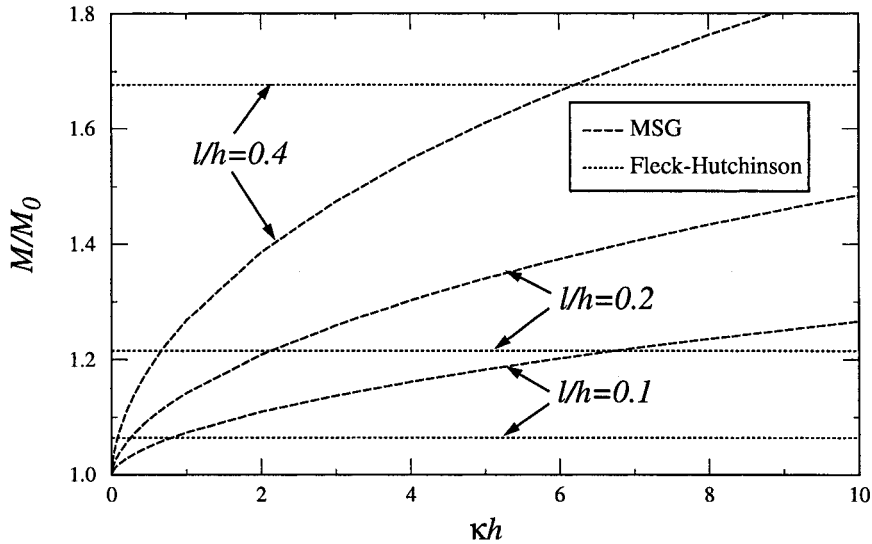

Fig. 2. The normalized bending moment, M/M_0, vs the normalized curvature, κh, for several ratios of intrinsic material length to beam thickness, l/h, where M_0 is the bending moment from classical plasticity, h is the beam thickness, and l is the intrinsic material length for mechanism-based strain gradient plasticity. Plastic work hardening exponent $N = 0.2$, shear modulus $\mu = 200\sigma_Y$, the coefficient α for Taylor's dislocation model $= 0.4$, and the ratio β of mesoscale cell size l_ϵ to dislocation spacing at plastic yielding is 10 for MSG plasticity (dashed lines). The dotted lines correspond to Fleck and Hutchinson's (1997) phenomenological strain gradient plasticity with intrinsic material lengths $l_1 = l/8$, $l_2 = l/2$, and $l_3 = l\sqrt{5/24}$.

size to dislocation spacing at plastic yielding are taken, $\beta = 1$ and $\beta = 10$. The results for the two values of β are indistinguishable in Fig. 1. The mesoscale cell size l_ϵ has virtually no effect on the moment over the range of parameters considered. Even at a ratio of $l/h = 2$, for which the beam thickness is half of the intrinsic material length and is on the order of microns, $\beta = 10$ corresponds to a mesoscale cell size more than one fifth of the beam thickness, yet the difference between $\beta = 1$ and $\beta = 10$ is still rather small. This is because the approximation of linear strain distribution within the mesoscale cell in MSG plasticity (Gao et al., 1999) is accurate for pure bending.

The bending moment M, normalized by its counterpart M_0 (κh) for classical plasticity, vs the normalized curvature κh is shown in Fig. 2 for several ratios of intrinsic material length to beam thickness, l/h, where the ratio of mesoscale cell size to dislocation spacing at plastic yielding is $\beta = 10$, and M_0 can be obtained from (29) by taking $l = 0$ and $l_\epsilon = 0$. The horizontal lines in Fig. 2 correspond to the bending moment estimated by Fleck and Hutchinson's (1997) phenomenological strain gradient plasticity since both M and M_0 are proportional to κ^N. The intrinsic material lengths in phenomenological strain gradient plasticity are $l_1 = l/8$, $l_2 = l/2$, and $l_3 = l\sqrt{5/24}$, as suggested by Begley and Hutchinson (1998), where l_i's are defined in Part I (Gao et al., 1999). This combination of material lengths for phenomenological strain gradient plasticity and $\beta = 10$ for MSG plasticity are also used in all of the following comparisons between two strain gradient plasticity theories. As far as bending is concerned, it appears that the MSG representation significantly underestimates the plastic work hardening reported by Stolken and Evans (1998) at small curvatures κ, which displays relatively large moment increases due to strain gradients in the range of small κ. However, this is reversed at large curvatures, i.e. MSG plasticity gives a larger bending moment than phenomenological strain gradient plasticity when the curvature is large. This is because the flow stresses are different in two theories. In phenomenological strain gradient plasticity, the flow stress is obtained from the uniaxial stress–strain relation (14) by replacing the strain ϵ with a combined measure of effective strain and effective strain gradient $\sqrt{\epsilon^2 + l^2\eta^2}$. The flow stress in MSG plasticity, however, is given in (16). The strain gradient term $l\eta$ in (16) is proportional to κ, while $f^2(\epsilon)$ is proportional to κ^{2N}. Therefore, the flow stress at a large curvature in MSG plasticity is on the order of $\sqrt{\kappa}$, while the flow stress in phenomenological strain gradient plasticity is only on the order of κ^N and is smaller. However, at an infinitesimal curvature, both flow stresses are on the order of κ^N because the strain gradient term $l\eta$ becomes negligible in (16), such that the flow stress in phenomenological strain gradient plasticity becomes larger.

3. Torsion of thin wires

Fleck et al. (1994) observed in twisting of thin copper wires that the scaled

shear strength increases significantly as the wire diameter decreases from 170 to 12 μ, whereby the shear flow strength of the thinnest wires is about three times of that of the thickest wires. However, no size dependence is observed in the tension tests, which induce no strain gradient. Here again, this size effect in torsion cannot be explained by classical plasticity, which involves no intrinsic material length. In this section, we use MSG plasticity to investigate torsion of thin wires.

The Cartesian reference frame is set such that the x_1 and x_2 axes are within the cross section of the wire, while the x_3 axis coincides with the central axis of the wire. The twist per unit length is designated κ and the radius of the wire is designated a. The displacement field is $u_1 = -\kappa x_2 x_3$, $u_2 = \kappa x_1 x_3$, $u_3 = 0$. The non-vanishing strains and strain gradients in the Cartesian reference frame and the effective strain ϵ and effective strain gradient η are given by

$$\epsilon_{13} = \epsilon_{31} = -\frac{\kappa}{2}x_2, \quad \epsilon_{23} = \epsilon_{32} = \frac{\kappa}{2}x_1, \quad \epsilon = \frac{1}{\sqrt{3}}\kappa r, \tag{30}$$

$$\eta_{231} = \eta_{321} = -\kappa, \quad \eta_{132} = \eta_{312} = \kappa, \quad \eta = \kappa, \tag{31}$$

where $r = \sqrt{x_1^2 + x_2^2}$ is the radius in polar coordinates (r, θ).

The constitutive Eqs. (19) and (20) give non-vanishing deviatoric stresses and higher-order stresses as

$$\sigma'_{13} = \sigma'_{31} = \frac{2\epsilon_{13}}{3\epsilon}\sigma, \quad \sigma'_{23} = \sigma'_{32} = \frac{2\epsilon_{23}}{3\epsilon}\sigma; \tag{32}$$

$$-\tau'_{113} = \tau'_{223} = -2\tau'_{311} = -2\tau'_{131} = 2\tau'_{322} = 2\tau'_{232} = \frac{\kappa l_\epsilon^2}{36}\frac{x_1 x_2}{r^2}\left[\frac{\sigma_Y^2 f(\epsilon)f'(\epsilon)}{\sigma} - \frac{\sigma}{\epsilon}\right],$$

$$\tau'_{123} = \tau'_{213} = \frac{\kappa l_\epsilon^2}{72}\frac{x_1^2 - x_2^2}{r^2}\left[\frac{\sigma_Y^2 f(\epsilon)f'(\epsilon)}{\sigma} - \frac{\sigma}{\epsilon}\right],$$

$$\tau'_{132} = \tau'_{312} = \frac{\kappa l_\epsilon^2}{72}\left[\frac{x_1^2}{r^2}\frac{\sigma_Y^2 f(\epsilon)f'(\epsilon)}{\sigma} + \frac{x_2^2}{r^2}\frac{\sigma}{\epsilon}\right],$$

$$\tau'_{231} = \tau'_{321} = -\frac{\kappa l_\epsilon^2}{72}\left[\frac{x_2^2}{r^2}\frac{\sigma_Y^2 f(\epsilon)f'(\epsilon)}{\sigma} + \frac{x_1^2}{r^2}\frac{\sigma}{\epsilon}\right]; \tag{33}$$

where σ is the flow stress given in (16), and l_ϵ is the mesoscale cell size in (23).

The equilibrium Eq. (6) and traction-free boundary conditions on the lateral surface of the wire $(r = a)$ give a vanishing hydrostatic stress, i.e.

$$H = 0. \tag{34}$$

The double-stress traction $\hat{r}_k$ in the cross section of the wire is zero, while the non-

vanishing stress tractions are

$$\hat{t}_1 = \sigma'_{31} - 2\frac{d\tau'_{311}}{dx_1} - 2\frac{d\tau'_{321}}{dx_2}, \quad \hat{t}_2 = \sigma'_{32} - 2\frac{d\tau'_{312}}{dx_1} - 2\frac{d\tau'_{322}}{dx_2}.$$

There is a line traction along the circumferential (θ) direction at the edge between the cross section and lateral surface ($r = a$) of the wire, given by

$$\hat{p}_\theta = \frac{\kappa l_\epsilon^2}{36} \frac{\sigma_Y^2 f(\epsilon) f'(\epsilon)}{\sigma}.$$

These stress and line tractions give a pure torque T, i.e. there are no net forces or bending moments in the cross section. The torque T can be obtained from the integration over the cross section of torques induced by these tractions as

$$T = \frac{2}{3}\pi\kappa \int_0^a r\left[\left(r^2 + \frac{l_\epsilon^2}{12}\right)\frac{\sigma}{\epsilon} + \frac{l_\epsilon^2}{12}\frac{\sigma_Y^2 f(\epsilon) f'(\epsilon)}{\sigma}\right] dr. \tag{35}$$

This torque vs twist-per-unit-length relation can also be obtained from the principle of virtual work by enforcing the equality of interval virtual work done
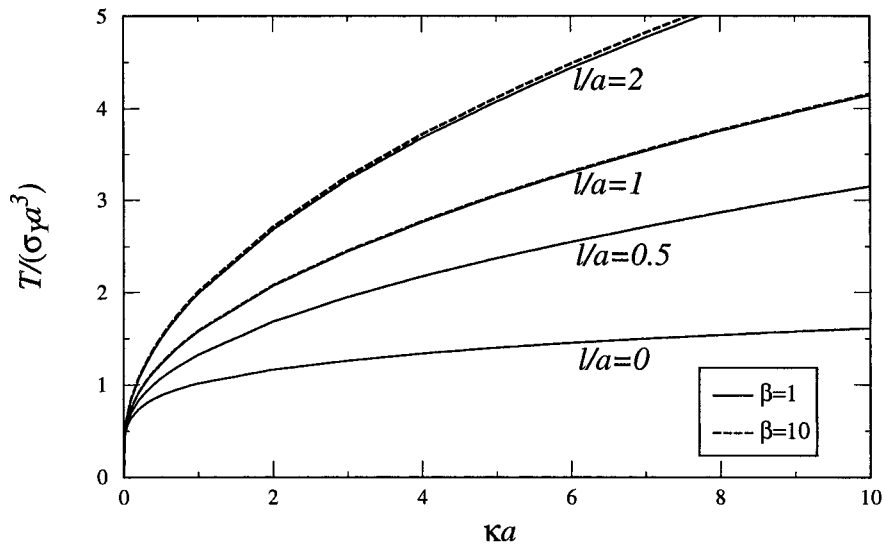

Fig. 3. The normalized torque, $T/(\sigma_Y a^3)$, vs the normalized twist per unit length, κa, for several ratios of intrinsic material length to wire radius, l/a, where σ_Y is the yield stress, a is the wire radius, and l is the intrinsic material length for mechanism-based strain gradient plasticity. The limit $l/a = 0$ corresponds to classical plasticity. Plastic work hardening exponent $N = 0.2$, shear modulus $\mu = 200\sigma_Y$, the coefficient α for Taylor's dislocation model $= 0.4$, and the ratio β of mesoscale cell size l_ϵ to dislocation spacing at plastic yielding is 1 for solid lines and 10 for dashed lines.

by stresses and higher-order stresses in the wire and external virtual work done by the torque, as detailed in Fleck and Hutchinson (1997).

The normalized torque, $T/(\sigma_Y a^3)$, vs the normalized twist per unit length, κa, is shown in Fig. 3 for several ratios of intrinsic material length to wire radius, l/a. The limit $l/a = 0$ corresponds to classical plasticity. Once again, in order to investigate the sensitivity to the mesoscale cell size, l_ϵ, two ratios of cell size to dislocation spacing at plastic yielding are taken, $\beta = 1$ and $\beta = 10$. It is observed that the torque-twist relation is rather insensitive to the parameter β, as well as to the mesoscale cell size l_ϵ. When $l/a = 2$, the wire radius is half of the intrinsic material length and is on the order of microns, and $\beta = 10$ corresponds to a mesoscale cell size more than one fifth of the wire radius; nevertheless, the difference between $\beta = 1$ and $\beta = 10$ is still rather small. This indicates that, even though the strain distribution (in a Cartesian reference frame) is not linear in torsion, MSG plasticity still gives a rather weak dependence on the mesoscale cell size.

It can be seen from Fig. 3 that the increase in plastic work hardening for a thin wire under torsion is slightly smaller than that observed in Fleck et al.'s (1994)
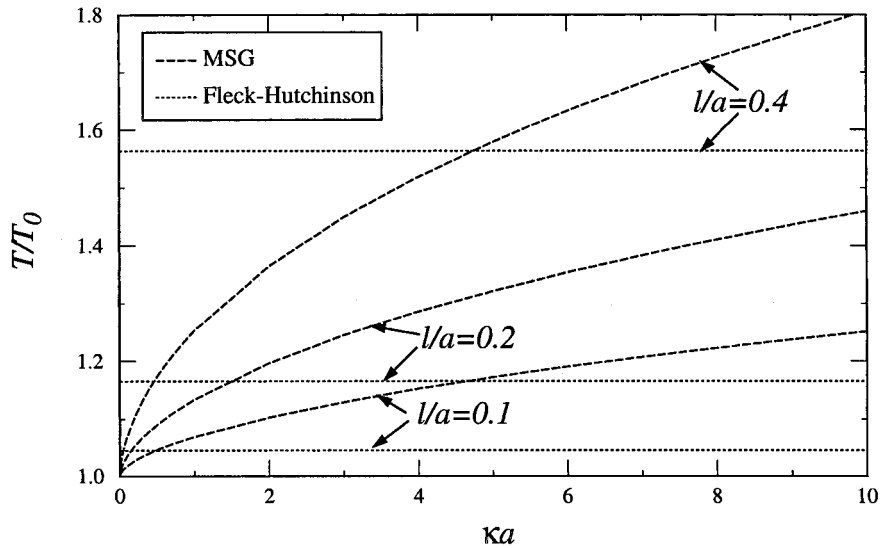

Fig. 4. The normalized torque, T/T_0, vs the normalized twist per unit length, κa, for several ratios of intrinsic material length to wire radius, l/a, where T_0 is the torque from classical plasticity, a is the wire radius, and l is the intrinsic material length for mechanism-based strain gradient plasticity. Plastic work hardening exponent $N = 0.2$, shear modulus $\mu = 200\sigma_Y$, the coefficient α for Taylor's dislocation model $= 0.4$, and the ratio β of mesoscale cell size l_ϵ to dislocation spacing at plastic yielding is 10 for MSG plasticity (dashed lines). The dotted lines correspond to Fleck and Hutchinson's (1997) phenomenological strain gradient plasticity with intrinsic material lengths $l_1 = l/8$, $l_2 = l/2$, and $l_3 = l\sqrt{5/24}$.

experiments. For example, the torque for $l/a = 1$ is approximately twice of that of classical plasticity ($l/a = 0$), and is smaller than the increase in shear flow strength by a factor of two to three for the thinnest wires in Fleck et al.'s experiments (1994).

The torque T, normalized by its counterpart T_0 (κa) for classical plasticity, vs the normalized twist per unit length κa is shown in Fig. 4 for several ratios of intrinsic material length to wire radius, l/a, where T_0 can be obtained from (35) by taking $l = 0$ and $l_\epsilon = 0$. The horizontal lines in Fig. 4 correspond to the torque estimated by Fleck and Hutchinson's (1997) phenomenological strain gradient plasticity since both T and T_0 are proportional to κ^N. As far as torsion is concerned, it appears that the MSG representation underestimates the plastic work hardening at small twists per unit length κ reported by Fleck et al. (1994), which displays relatively large torque increases due to strain gradients in the range of small κ. It is observed that phenomenological strain gradient plasticity gives a larger torque than MSG plasticity at small twists per unit length, but this is reversed when the twist per unit length becomes large, consistent with Fig. 2 for bending moment. This is once again due to the difference in flow stress in two theories.

4. Void growth: the role of void size

The nucleation, growth and coalescence of microvoids is a common fracture mechanism of ductile metals. Though there have been significant studies on the mechanics of void growth based on classical plasticity theory (e.g. Rice and Tracy, 1969; Gurson, 1977; Tvergaard, 1990; Huang, 1991; Needleman et al., 1992), these studies do not show any dependence on void size since classical plasticity theories do not involve an intrinsic material length. It is therefore of interest to investigate the effect of void size on the void growth phenomena, particularly for micron- and submicron-sized voids. In this section, we use MSG plasticity to investigate the following two simplest cases: (1) growth of a spherical void in an infinite medium subjected to remote spherically symmetric tension, and (2) growth of a cylindrical void in an infinite medium subjected to remote equi-biaxial tension.

4.1. Growth of spherical voids

A spherical void of initial radius R_0 in an infinite medium is subjected to remote spherically symmetric tension, σ^∞. The spherical coordinates (R, θ, ϕ) are used. The solid is incompressible, so that the non-vanishing displacement in spherical coordinates is

$$u_\mathrm{R} = \frac{R_0^2}{R^2} u_0, \tag{36}$$

where u_0 is the displacement on the void surface. The non-vanishing strains and strain gradients in spherical coordinates are

$$\epsilon_{RR} = -2\epsilon_{\theta\theta} = -2\epsilon_{\phi\phi} = -2\frac{R_0^2}{R^3}u_0, \tag{37}$$

$$\eta_{RRR} = -2\eta_{R\theta\theta} = -2\eta_{\theta R\theta} = -2\eta_{R\phi\phi} = -2\eta_{\phi R\phi} = -2\eta_{\theta\theta R} = -2\eta_{\phi\phi R}$$

$$= 6\frac{R_0^2}{R^4}u_0. \tag{38}$$

The effective strain ϵ and effective strain gradient η are given by

$$\epsilon = 2\frac{R_0^2}{R^3}u_0, \quad \eta = 3\sqrt{\frac{5}{2}}\frac{R_0^2}{R^4}u_0. \tag{39}$$

The constitutive Eqs. (19) and (20) give non-vanishing deviatoric stresses and higher-order stresses as

$$\sigma'_{RR} = -2\sigma'_{\theta\theta} = -2\sigma'_{\phi\phi} = -\frac{2}{3}\sigma; \tag{40}$$

$$\tau'_{RRR} = -2\tau'_{R\theta\theta} = -2\tau'_{\theta R\theta} = -2\tau'_{R\phi\phi} = -2\tau'_{\phi R\phi} = \frac{l_\epsilon^2}{12}\frac{R_0^2}{R^4}u_0\left[\frac{3\sigma_Y^2 f(\epsilon)f'(\epsilon)}{\sigma} + \frac{\sigma}{\epsilon}\right],$$

$$\tau'_{\theta\theta R} = \tau'_{\phi\phi R} = -\frac{l_\epsilon^2}{6}\frac{R_0^2}{R^4}u_0\frac{\sigma}{\epsilon}; \tag{41}$$

where σ is the flow stress given in (16), and l_ϵ is the mesoscale cell size in (23).

The equilibrium Eq. (6) and traction-free boundary conditions on the void surface ($R = R_0$) give the hydrostatic stress H as

$$H = \frac{d\tau'_{RRR}}{dR} + \frac{2}{R}(2\tau'_{RRR} - 2\tau'_{R\theta\theta} - \tau'_{\theta\theta R}) - \sigma'_{RR}$$

$$+ 2\int_{R_0}^{R}\left(3\frac{\tau'_{RRR} - 2\tau'_{R\theta\theta} - \tau'_{\theta\theta R}}{R^2} - \frac{\sigma'_{RR} - \sigma'_{\theta\theta}}{R}\right)dR. \tag{42}$$

As R approaches infinity, all deviatoric stresses and higher-order stresses vanish, such that (42) gives the remotely applied spherically symmetric stress,

$$\sigma^\infty = 2\int_{R_0}^{\infty}\left(3\frac{\tau'_{RRR} - 2\tau'_{R\theta\theta} - \tau'_{\theta\theta R}}{R^2} - \frac{\sigma'_{RR} - \sigma'_{\theta\theta}}{R}\right)dR. \tag{43}$$

The substitution of deviatoric stresses and higher-order stresses in (40) and (41) into the above expression gives

$$\sigma^\infty = 2\int_{R_0}^{\infty}\left[\frac{\sigma}{R} + \frac{l_\epsilon^2}{2}\frac{R_0^2}{R^6}u_0\left(\frac{2\sigma}{\epsilon} + \frac{3\sigma_Y^2 f(\epsilon)f'(\epsilon)}{\sigma}\right)\right]\,dR. \tag{44}$$

The remotely applied stress, σ^∞, normalized by the yield stress σ_Y, vs the normalized displacement on the void surface, u_0/R_0, is shown in Fig. 5 for several ratios of intrinsic material length to initial void radius, l/R_0. The limit $l/R_0 = 0$ corresponds to classical plasticity, while $l/R_0 = 2$ and $l/R_0 = 5$ correspond to micron-sized voids since the intrinsic material length l is on the order of microns (e.g. 5 μ for copper). It is observed that, for micron-sized voids (e.g. $l/R_0 = 2$ and 5), the void growth is rather insensitive to the parameter β, as well as to the mesoscale cell size l_ϵ. The difference between $\beta = 1$ and $\beta = 10$ is slightly larger than those in Figs. 1 and 3, because $l/R_0 = 5$ and $\beta = 10$ corresponds to a relatively large mesoscale cell size, more than half of the initial radius of the void. This supports the conclusions established from the previous sections for bending and torsion that MSG plasticity predicts a rather weak dependence on the mesoscale cell size.

It is also observed from Fig. 5 that the curves for $l/R_0 = 0$, 2 and 5 are rather close. For example, the curve for $l/R_0 = 5$ is no more than 25% higher than the

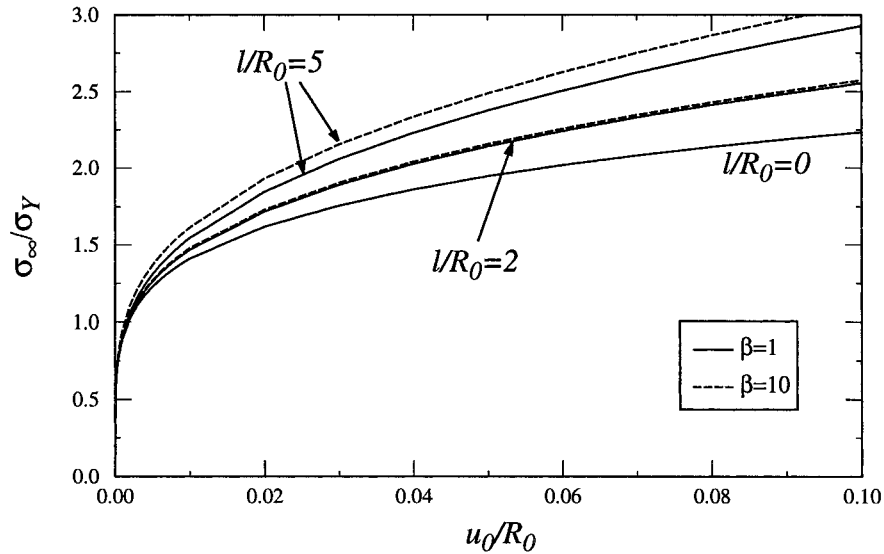Fig. 5. The remotely applied stress, σ^∞, normalized by the yield stress σ_Y, vs the normalized displacement on the surface of a spherical void, u_0/R_0, for several ratios of intrinsic material length to initial void radius, l/R_0, where R_0 is the initial radius of the void, and l is the intrinsic material length for mechanism-based strain gradient plasticity. The limit $l/R_0 = 0$ corresponds to classical plasticity. Plastic work hardening exponent $N = 0.2$, shear modulus $\mu = 200\sigma_Y$, the coefficient α for Taylor's dislocation model $= 0.4$, and the ratio β of mesoscale cell size l_ϵ to dislocation spacing at plastic yielding is 1 for solid lines and 10 for dashed lines.

prediction by classical plasticity ($l/R_0 = 0$). Therefore, MSG plasticity predicts small effects of the radius of micron-sized voids on their growth. However, we must point out that this conclusion is limited to micron-sized voids. In fact, for submicron-sized voids (e.g. $l/R_0 \geq 20$), we have found that the corresponding curves are much higher than those in Fig. 5, indicating the submicron-sized voids are much less susceptible to growth at a given stress state than larger voids.

The remotely applied stress σ^{∞}, normalized by its counterpart $(\sigma^{\infty})_0$ for classical plasticity, vs the normalized displacement u_0/R_0 on the void surface is shown in Fig. 6 for a micron-sized void ($l/R_0 = 1$) and a submicron-sized void ($l/R_0 = 10$), where $(\sigma^{\infty})_0$ can be obtained from (44) by taking $l = 0$ and $l_\epsilon = 0$. The horizontal lines in Fig. 6 correspond to the remotely applied stress estimated by Fleck and Hutchinson's (1997) phenomenological strain gradient plasticity. For a micron-sized void ($l/R_0 = 1$), the difference between two theories are relatively small. For a submicron-sized void ($l/R_0 = 10$), the phenomenological strain gradient plasticity gives a larger remotely applied stress than MSG plasticity in the
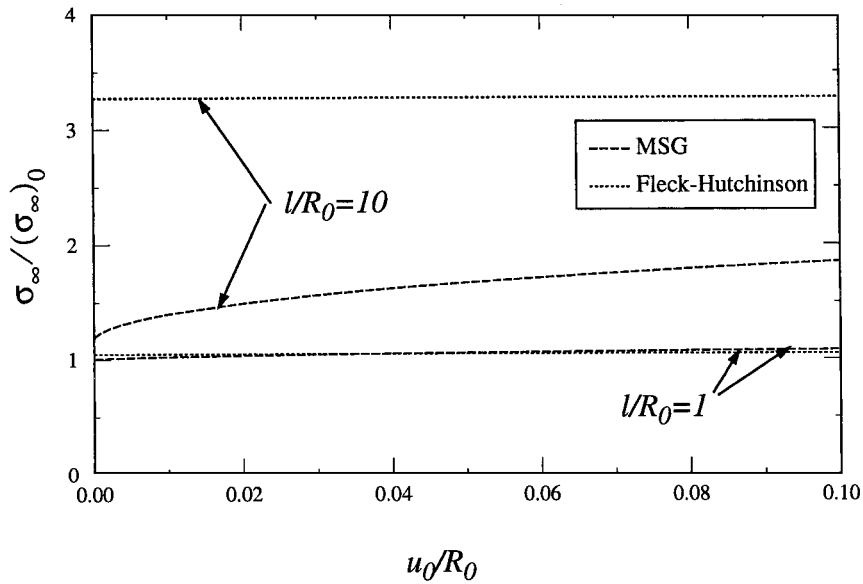

Fig. 6. The remotely applied stress, σ^{∞}, normalized by the counterpart in classical plasticity, $(\sigma^{\infty})_0$, vs the normalized displacement on the surface of a spherical void, u_0/R_0, for several ratios of intrinsic material length to initial void radius, l/R_0, where R_0 is the initial radius of the void, and l is the intrinsic material length for mechanism-based strain gradient plasticity. Plastic work hardening exponent $N = 0.2$, shear modulus $\mu = 200\sigma_Y$, the coefficient α for Taylor's dislocation model $= 0.4$, and the ratio β of mesoscale cell size l_ϵ to dislocation spacing at plastic yielding is 10 for MSG plasticity (dashed lines). The dotted lines correspond to Fleck and Hutchinson's (1997) phenomenological strain gradient plasticity with intrinsic material lengths $l_1 = l/8$, $l_2 = l/2$, and $l_3 = l\sqrt{5/24}$.

range of displacement on the void surface shown in Fig. 6. The differences between the two theories, however, decrease as the void grows.

4.2. Growth of cylindrical voids

A cylindrical void of initial radius r_0 in an infinite medium is subjected to remote equi-biaxial tension, $\sigma_{11}^{\infty} = \sigma_{22}^{\infty} = \sigma^{\infty}$. The cylindrical coordinates (r, θ, z) are used, where the z axis coincides with the central axis of the void. The solid is incompressible and is under plane-strain deformation, such that the non-vanishing displacement is $u_r = (r_0/r)u_0$, where u_0 is the displacement on the void surface. The non-vanishing strains and strain gradients in cylindrical coordinates and the effective strain ϵ and effective strain gradient η are given by

$$\epsilon_{rr} = -\epsilon_{\theta\theta} = -\frac{r_0}{r^2}u_0, \quad \epsilon = \frac{2}{\sqrt{3}}\frac{r_0}{r^2}u_0, \tag{45}$$

$$\eta_{rrr} = -\eta_{r\theta\theta} = -\eta_{\theta r\theta} = -\eta_{\theta\theta r} = 2\frac{r_0}{r^3}u_0, \quad \eta = 2\frac{r_0}{r^3}u_0. \tag{46}$$

The constitutive Eqs. (19) and (20) give non-vanishing deviatoric stresses and higher-order stresses as

$$\sigma_{rr}' = -\sigma_{\theta\theta}' = -\frac{1}{\sqrt{3}}\sigma; \tag{47}$$

$$\tau_{rrr}' = \frac{l_\epsilon^2}{36}\frac{r_0}{r^3}u_0\left[\frac{3\sigma_Y^2 f(\epsilon)f'(\epsilon)}{\sigma} + \frac{\sigma}{\epsilon}\right],$$

$$\tau_{r\theta\theta}' = \tau_{\theta r\theta}' = -\frac{l_\epsilon^2}{72}\frac{r_0}{r^3}u_0\left[\frac{5\sigma_Y^2 f(\epsilon)f'(\epsilon)}{\sigma} + \frac{3\sigma}{\epsilon}\right],$$

$$\tau_{\theta\theta r}' = -\frac{l_\epsilon^2}{9}\frac{r_0}{r^3}u_0\frac{\sigma}{\epsilon},$$

$$\tau_{rzz}' = \tau_{zrz}' = -\frac{l_\epsilon^2}{72}\frac{r_0}{r^3}u_0\left[\frac{\sigma_Y^2 f(\epsilon)f'(\epsilon)}{\sigma} - \frac{\sigma}{\epsilon}\right]; \tag{48}$$

where σ is the flow stress given in (16), and l_ϵ is the mesoscale cell size in (23).

The equilibrium Eq. (6) and traction-free boundary conditions on the void surface ($r = r_0$) give the hydrostatic stress H as

$$H = \frac{d\tau'_{rr}}{dr} + \frac{1}{r}(2\tau'_{rr} - 2\tau'_{r\theta\theta} - \tau'_{\theta\theta r}) - \sigma'_{rr}$$

$$+ \int_{r_0}^{r} \left(2\frac{\tau'_{rr} - 2\tau'_{r\theta\theta} - \tau'_{\theta\theta r}}{r^2} - \frac{\sigma'_{rr} - \sigma'_{\theta\theta}}{r} \right) dr. \tag{49}$$

As r approaches infinity, all deviatoric stresses and higher-order stresses vanish, such that (49) gives the remotely applied equi-biaxial stress,

$$\sigma^\infty = \int_{r_0}^{\infty} \left(2\frac{\tau'_{rr} - 2\tau'_{r\theta\theta} - \tau'_{\theta\theta r}}{r^2} - \frac{\sigma'_{rr} - \sigma'_{\theta\theta}}{r} \right) dr. \tag{50}$$

The substitution of deviatoric stresses and higher-order stresses in (47) and (48) into the above expression gives

$$\sigma^\infty = \frac{2}{\sqrt{3}} \int_{2_0}^{\infty} \left[\frac{\sigma}{r} + \frac{2l_\epsilon^2}{3\sqrt{3}} \frac{r_0}{r^5} u_0 \left(\frac{\sigma}{\epsilon} + \frac{\sigma_Y^2 f(\epsilon) f'(\epsilon)}{\sigma} \right) \right] dr. \tag{51}$$

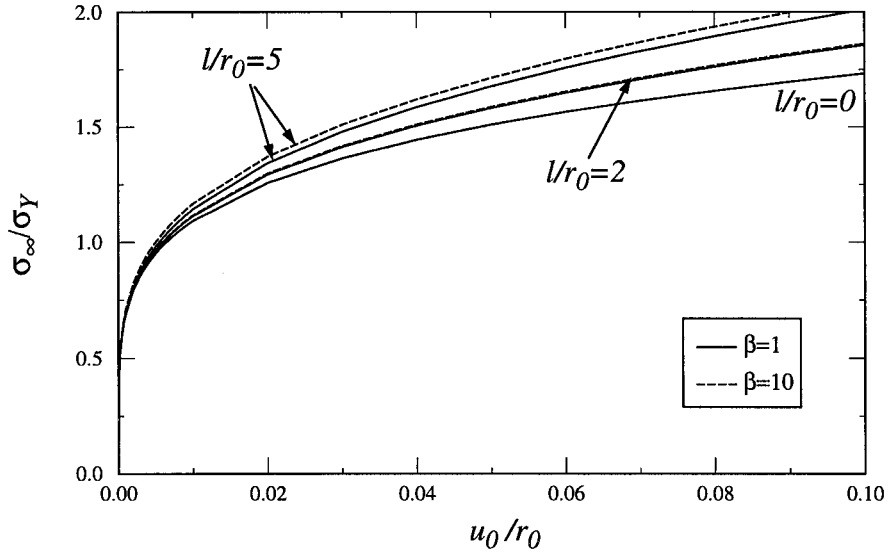The remotely applied stress, σ^∞, normalized by the yield stress σ_Y, vs the

Fig. 7. The remotely applied stress, σ^∞, normalized by the yield stress σ_Y, vs the normalized displacement on the surface of a cylindrical void, u_0/r_0, for several ratios of intrinsic material length to initial void radius, l/r_0, where r_0 is the initial radius of the void, and l is the intrinsic material length for mechanism-based strain gradient plasticity. The limit $l/r_0 = 0$ corresponds to classical plasticity. Plastic work hardening exponent $N = 0.2$, shear modulus $\mu = 200\sigma_Y$, the coefficient α for Taylor's dislocation model $= 0.4$, and the ratio β of mesoscale cell size l_ϵ to dislocation spacing at plastic yielding is 1 for solid lines and 10 for dashed lines.

normalized displacement on the void surface, u_0/r_0, is shown in Fig. 7 for several ratios of intrinsic material length to initial void radius, l/r_0. Once again, it is observed that void growth is rather insensitive to the parameter β, as well as to the mesoscale cell size l_ϵ, for micron-sized voids. Since curves in Fig. 7 are rather close, it is found that MSG plasticity predicts little effect of the void radius of micron-sized voids on their growth.

5. Cavitation instabilities

A void in an elastic-plastic solid will grow unstably at sufficiently high mean stresses, a phenomenon called cavitation instability (Bishop et al., 1945; Huang et al., 1991). Fleck and Hutchinson (1997) investigated the effect of void size on cavitation instability by the phenomenological strain gradient plasticity, and established that strain gradients delay cavitation to larger mean stresses when the void size is on the order of microns. In this section, we investigate cavitation instability in mechanism-based strain gradient plasticity.

A spherical void in an infinite, incompressible solid is subjected to remote triaxial tension. Since cavitation instabilities are dominated by a very high mean stress, we can simplify the remote stress state to a spherically symmetric tension, σ^∞. The spherical coordinates (R, θ, ϕ) in the initial configuration and (r, θ, ϕ) in the current configuration are used, where we use R to designate the initial radius of a material point in the undeformed configuration, and r to denote the current radius of the same material point in the deformed configuration. The void radius is denoted by R_0 and r_0 in the initial and current configurations, respectively. It is important to distinguish between these two configurations because finite strain effects play a crucial role in cavitation instability.

Cavitation is driven by the elastic energy stored in the remote field (Huang et al., 1991); therefore it is essential to include elasticity in the constitutive model. We use the following elastic-power-law-hardening uniaxial stress–strain relation to replace that in (15),

$$f(\epsilon) = \frac{E\epsilon}{\sigma_Y} \quad \text{if} \quad \epsilon \leq \frac{\sigma_Y}{E}$$

$$f(\epsilon) = \left(\frac{E\epsilon}{\sigma_Y}\right)^N \quad \text{if} \quad \epsilon > \frac{\sigma_Y}{E}, \tag{52}$$

where E is the Young's modulus.

The incompressibility of the solid requires

$$R^3 - R_0^3 = r^3 - r_0^3. \tag{53}$$

Its derivative with respect to time gives the particle velocity in the current

configuration,

$$v_r = \dot{r} = \frac{r_0^2}{r^2} \dot{r}_0, \tag{54}$$

where $\dot{r}_0$ is the velocity of the void surface. The strain rates in the current configuration are

$$\dot{\epsilon}_{rr} = \frac{dv_r}{dr}, \quad \dot{\epsilon}_{\theta\theta} = \dot{\epsilon}_{\phi\phi} = \frac{v_r}{r}. \tag{55}$$

Because the velocity field is irrotational, we may integrate the strain rate tensor with respect to time to obtain strains in finite deformation as

$$\epsilon_{rr} = -2 \ln \frac{r}{R}, \quad \epsilon_{\theta\theta} = \epsilon_{\phi\phi} = \ln \frac{r}{R}. \tag{56}$$

It is observed that the above expressions for strains are identical to logarithmic true strains defined by Huang et al. (1991) for a spherically symmetric problem. Similarly, the rates of strain gradients in the current configuration are given in terms of the velocity field by

$$\dot{\eta}_{rrr} = \frac{d^2 v_r}{dr^2}, \quad \dot{\eta}_{r\theta\theta} = \dot{\eta}_{\theta r\theta} = \dot{\eta}_{r\phi\phi} = \dot{\eta}_{\phi r\phi} = \dot{\eta}_{\theta\theta r} = \dot{\eta}_{\phi\phi r} = \frac{d}{dr}\left(\frac{v_r}{r}\right). \tag{57}$$

Accordingly, the integration of rates of strain gradients with respect to time gives strain gradients in finite deformation,

$$\eta_{rrr} = 6\left(\frac{1}{R} - \frac{1}{r}\right),$$

$$\eta_{r\theta\theta} = \eta_{\theta r\theta} = \eta_{r\phi\phi} = \eta_{\phi r\phi} = \eta_{\theta\theta r} = \eta_{\phi\phi r} = -3\left(\frac{1}{R} - \frac{1}{r}\right). \tag{58}$$

The effective strain ϵ and effective strain gradient η are given by

$$\epsilon = 2 \ln\left(\frac{r}{R}\right) = \frac{2}{3} \ln\left(\frac{r^3}{r^3 - r_0^3 + R_0^3}\right),$$

$$\eta = 3\sqrt{\frac{5}{2}}\left(\frac{1}{R} - \frac{1}{r}\right) = 3\sqrt{\frac{5}{2}}\left[\frac{1}{(r^3 - r_0^3 + R_0^3)^{1/3}} - \frac{1}{r}\right], \tag{59}$$

where the radius R of the material point in the initial, undeformed configuration has been eliminated by (53).

The constitutive Eqs. (19) and (20) give non-vanishing deviatoric true stresses and true higher-order stresses in the current configuration

$$\sigma'_{\text{rr}} = -2\sigma'_{\theta\theta} = -2\sigma'_{\phi\phi} = -\frac{2}{3}\sigma; \tag{60}$$

$$\tau'_{\text{rrr}} = -2\tau'_{\text{r}\theta\theta} = -2\tau'_{\theta\text{r}\theta} = -2\tau'_{\text{r}\phi\phi} = -2\tau'_{\phi\text{r}\phi}$$

$$= \frac{l_\epsilon^2}{12}\left(\frac{1}{R} - \frac{1}{r}\right)\left[\frac{3\sigma_{\text{Y}}^2 f(\epsilon)f'(\epsilon)}{\sigma} + \frac{\sigma}{\epsilon}\right],$$

$$\tau'_{\theta\theta\text{r}} = \tau'_{\phi\phi\text{r}} = -\frac{l_\epsilon^2}{6}\left(\frac{1}{R} - \frac{1}{r}\right)\frac{\sigma}{\epsilon}; \tag{61}$$

where σ is the flow stress given in (16), and l_ϵ is the mesoscale cell size in (23).

The equilibrium Eq. (6) can be written in terms of σ'_{ij}, τ'_{ijk}, and the hydrostatic stress H as
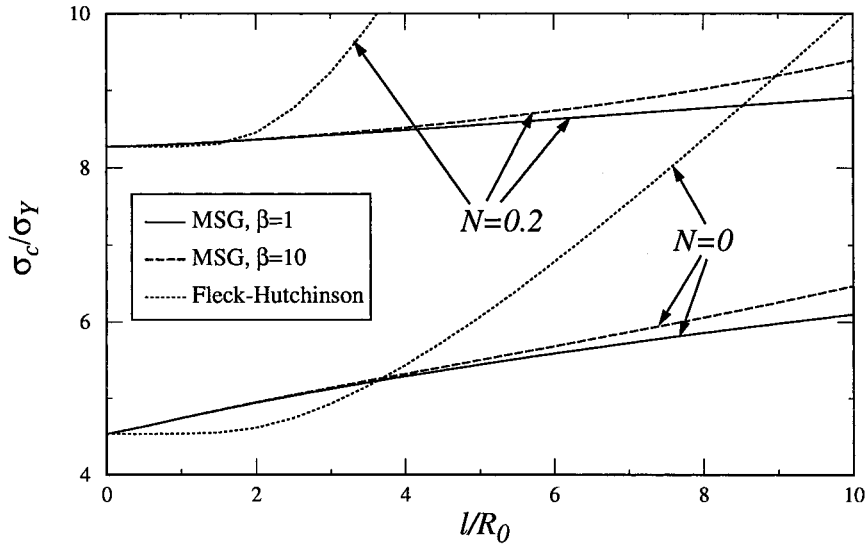

Fig. 8. The cavitation stress, σ_{c}, normalized by the yield stress σ_{Y}, vs the ratio of intrinsic material length to initial void radius, l/R_0, where R_0 is the initial radius of the void, and l is the intrinsic material length for mechanism-based strain gradient plasticity. The limit $l/R_0 = 0$ corresponds to classical plasticity. Plastic work hardening exponent $N = 0.2$ and $N = 0$, Young's modulus $E = 500\sigma_{\text{Y}}$, shear modulus $\mu = 200\sigma_{\text{Y}}$, the coefficient α for Taylor's dislocation model $= 0.4$, and the ratio β of mesoscale cell size l_ϵ to dislocation spacing at plastic yielding is 1 for solid lines and 10 for dashed lines in MSG plasticity. The dotted lines correspond to Fleck and Hutchinson's (1997) phenomenological strain gradient plasticity with intrinsic material lengths $l_1 = l/8$, $l_2 = l/2$, and $l_3 = l\sqrt{5/24}$.

$$\frac{dH}{dr} + \frac{d\sigma'_{rr}}{dr} + \frac{2}{r}(\sigma'_{rr} - \sigma'_{\theta\theta}) - \frac{d}{dr}\left[\frac{d\tau'_{rrr}}{dr} + \frac{2}{r}(\tau'_{rrr} - \tau'_{r\theta\theta} - \tau'_{\theta\theta r})\right]$$

$$- \frac{2}{r}\left[\frac{d}{dr}(\tau'_{rrr} - \tau'_{r\theta\theta}) + \frac{1}{r}(2\tau'_{rrr} - 5\tau'_{r\theta\theta} - 3\tau'_{\theta\theta r})\right] = 0. \tag{62}$$

The traction-free boundary conditions on the void surface in the current configuration give the value of H at $r = r_0$. Since all deviatoric stresses and higher-order stresses vanish in the remote field, the integration of (62) from the void surface ($r = r_0$) to infinity gives the remotely applied spherically symmetric stress as

$$\sigma^\infty = 2\int_{r_0}^{\infty}\left\{\frac{\sigma}{r} + \frac{l_\epsilon^2}{2r^2}\left[\frac{1}{(r^3 - r_0^3 + R_0^3)^{1/3}} - \frac{1}{r}\right]\left[\frac{2\sigma}{\epsilon} + \frac{3\sigma_Y^2 f(\epsilon)f'(\epsilon)}{\sigma}\right]\right\} dr. \tag{63}$$

This is the relation between the void radius, r_0, in the current configuration and the remotely applied stress, σ^∞. The numerical integration for (63) has shown that, as the void radius r_0 starts to increase from the initial void radius R_0, the remote stress σ^∞ also increases. However, when r_0 exceeds a critical value, typically from 1.3 to 3 times the initial void radius R_0, the remote stress σ^∞ begins to decrease as r_0 increases, i.e. there exists a maximum value of remote stress at which the void grows without bound ($dr_0/d\sigma^\infty \to \infty$). This maximum value of the remote stress is called the cavitation stress and is designated σ_c; it represents the intrinsic limit for mean stress in a material.

The cavitation stress, σ_c, normalized by the yield stress σ_Y, vs the ratio of intrinsic material length to initial void radius, l/R_0, is shown in Fig. 8. The limit $l/R_0 = 0$ corresponds to classical plasticity, while $l/R_0 = 1$ and $l/R_0 = 10$ correspond to a micron-sized void and a submicron-sized void, respectively, since the intrinsic material length l is on the order of microns. The plots show two values of the plastic work hardening exponent N, 0.2 and 0, where the latter corresponds to an elastic-perfectly plastic solid. The Young's modulus E is 500 times the yield stress σ_Y. It is observed that for both micron- and submicron-sized voids, the cavitation stress is rather insensitive to the parameter β, as well as to the mesoscale cell size l_ϵ.

Although strain gradient effects increase the cavitation stress, this increase in MSG plasticity is different from that in Fleck and Hutchinson's (1997) phenomenological strain gradient plasticity. The cavitation stress in phenomenological strain gradient plasticity with material lengths $l_1 = l/8$, $l_2 = l/2$, and $l_3 = l\sqrt{5/24}$ (Begley and Hutchinson, 1998) is also shown in Fig. 8. For an elastic-perfectly plastic solid ($N = 0$), MSG plasticity gives a slightly higher cavitation stress than phenomenological strain gradient plasticity when the void radius is larger than approximately one quarter of intrinsic material length l (i.e. micron-sized void). When the void size is reduced to submicron, however, the cavitation stress in phenomenological strain gradient plasticity increases rapidly and becomes much higher than that in MSG plasticity. For submicron-sized voids ($l/R_0 = 10$), the cavitation stress in MSG plasticity is approximately 40% larger

than the estimate based on classical plasticity, while the increase in phenomenological strain gradient plasticity is more than 100%. For an elastic-power law hardening solid ($N = 0.2$), the above observations also hold, except that the curve for MSG plasticity becomes more flat, while the curve for phenomenological strain gradient plasticity increases much more rapidly.

6. Bimaterials in shear

The studies in the previous sections all shared one feature, namely that the deformation field is known a priori except for a single amplitude factor, such as the curvature in bending, twist per unit length in torsion, or displacement on the void surface in void growth and cavitation instabilities. In this section, we study two problems whereby the deformation fields are not known a priori and can only be obtained numerically. First, a semi-infinite material bonded to a rigid substrate and subjected to remote shear. Second, an axisymmetric fiber embedded in an infinite matrix subjected to shear parallel to the fiber direction.

6.1. Bimaterial interfaces in shear

A semi-infinite solid is bonded to a rigid substrate and is subjected to remotely imposed pure shear. The Cartesian reference frame is set such that the interface between the solid and the rigid substrate coincides with the plane $x_2 = 0$, and the shear is parallel to the x_3 axis. The remote shear strain is designated ϵ_{23}^∞. For convenience, the remote engineering shear strain is designated γ^∞ ($= 2\epsilon_{23}^\infty$).

The only non-vanishing displacement is the displacement u_3, which depends only on the distance away from the interface, i.e. $u_3 = w(x_2)$. The non-vanishing strains and strain gradients in the Cartesian reference frame are

$$\epsilon_{23} = \epsilon_{32} = \frac{1}{2}\frac{\mathrm{d}w}{\mathrm{d}x_2}, \quad \eta_{223} = \frac{\mathrm{d}^2 w}{\mathrm{d}x_2^2}.$$

The effective strain ϵ and effective strain gradient η are given by

$$\epsilon = \frac{1}{\sqrt{3}}\frac{\mathrm{d}w}{\mathrm{d}x_2}, \quad \eta = \frac{1}{2}\frac{\mathrm{d}^2 w}{\mathrm{d}x_2^2}.$$

The constitutive Eqs. (19) and (20) give non-vanishing deviatoric stresses and higher-order stresses as

$$\sigma_{23}' = \sigma_{32}' = \frac{1}{\sqrt{3}}\sigma, \tag{64}$$

$$\tau'_{223} = -8\tau'_{311} = -8\tau'_{131} = \frac{8}{3}\tau'_{322} = \frac{8}{3}\tau'_{232} = -4\tau'_{333} = \frac{l_\epsilon^2}{36}\frac{d^2w}{dx_2^2}\frac{\sigma_Y^2 f(\epsilon)f'(\epsilon)}{\sigma}, \quad (65)$$

where σ is the flow stress given in (16), and l_ϵ is the mesoscale cell size in (23).

It can be verified from the equilibrium equation and traction-free condition of the normal stress in the x_3 direction that the hydrostatic stress H is zero, and the equilibrium Eq. (6) becomes

$$\frac{d\sigma'_{23}}{dx_2} - \frac{d^2\tau'_{223}}{dx_2^2} = 0. \quad (66)$$

The remote boundary conditions are

$$\sigma'_{23}(x_2\rightarrow\infty) = \sigma_{23}^\infty, \quad \tau'_{223}(x_2\rightarrow\infty) = 0, \quad (67)$$

where σ_{23}^∞ is the remotely applied shear stress. Since the solid is bonded to a rigid substrate, the displacement and rotation must vanish at the interface, so that

$$w = \frac{dw}{dx_2} = 0 \quad \text{at} \quad x_2 = 0. \quad (68)$$

It should be pointed out that the strain gradient effects come only from the higher-order boundary conditions at the interface in this example. In other words, the simple solution of uniform shear stress and strain would hold if the vanishing of rotation $dw/dx_2 = 0$ at $x_2 = 0$ were not imposed. This example illustrates the additional scope of the higher order theory in an essential way.

It can be shown that Eqs. (66)–(68) have the following perturbation solution:

$$w = w_0(x_2) + l_\epsilon^2 w_1(x_2) + l_\epsilon^4 w_2(x_2) + \cdots, \quad (69)$$

where the zeroth order perturbation solution w_0 is governed by

$$\frac{l}{2}\frac{d^2 w_0}{dx_2^2} + f^2(\epsilon_0) = \frac{3\sigma_{23}^{\infty 2}}{\sigma_Y^2}, \quad (70)$$

and the first order perturbation solution w_1 is governed by

$$\frac{l}{2}\frac{d^2 w_1}{dx_2^2} + \frac{2}{\sqrt{3}}f(\epsilon_0)f'(\epsilon_0)\frac{dw_1}{dx_2} = \frac{2}{\sqrt{3}}\frac{d}{dx_2}\left[f(\epsilon_0)f'(\epsilon_0)\frac{d^2 w_0}{dx_2^2}\right]. \quad (71)$$

Here l is the intrinsic material length in (18), f is the uniaxial stress–strain relation given in (52), and ϵ_0 is the effective strain for the zeroth order perturbation solution, i.e. $\epsilon_0 = (1/\sqrt{3}) dw_0/dx_2$.

The displacement near the interface, normalized by the remote engineering strain γ^∞ and the intrinsic material length l, vs the normalized distance to the interface, x_2/l, is shown in Fig. 9(a) for remote shear strain $\gamma^\infty = 0.1\gamma_Y$, where $\gamma_Y = \sqrt{3}\sigma_Y/E$ is the yield strain in pure shear. The Young's modulus E is 500
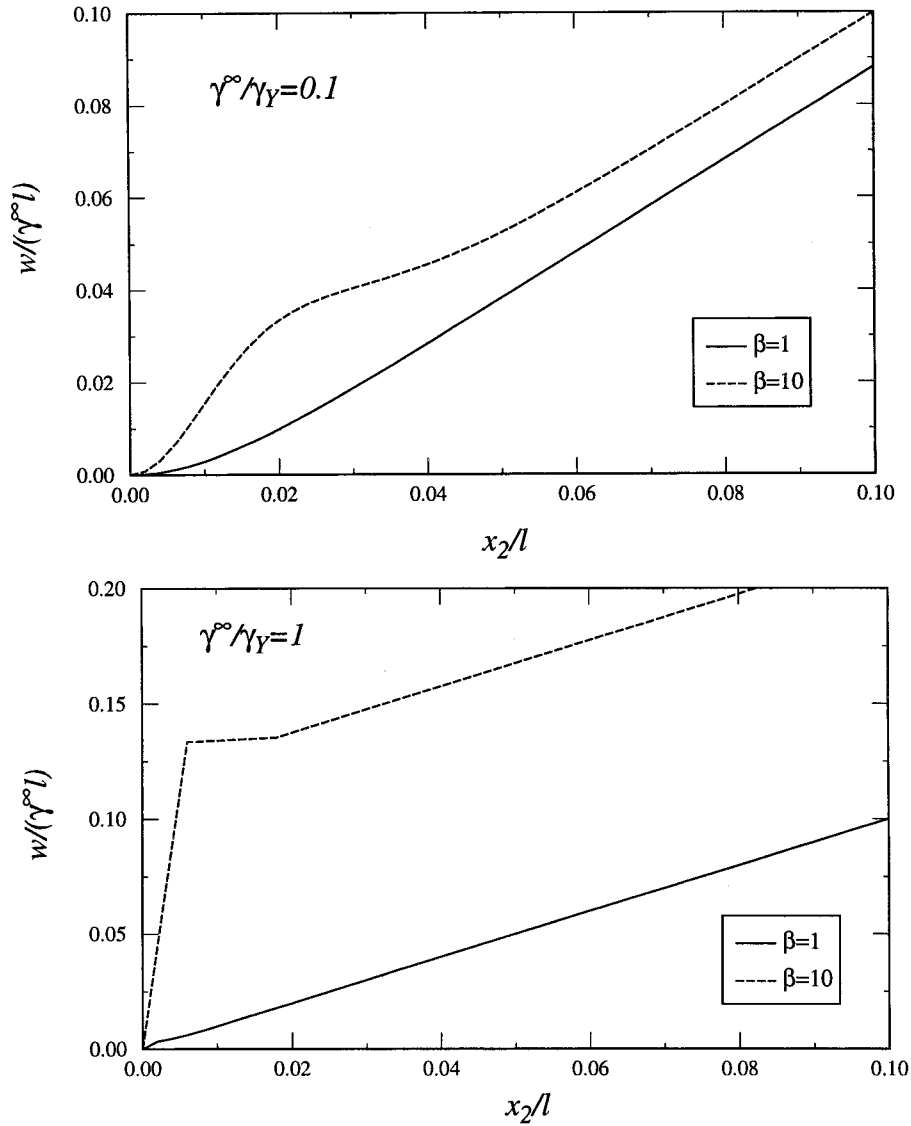
Fig. 9. The displacement near the interface, normalized by the remote engineering strain γ^∞ and the intrinsic material length l, vs the normalized distance to the interface, x_2/l. Plastic work hardening exponent $N = 0.2$, Young's modulus $E = 500\sigma_Y$, shear modulus $\mu = 200\sigma_Y$, the coefficient α for Taylor's dislocation model $= 0.4$, and the ratio β of mesoscale cell size l_ϵ to dislocation spacing at plastic yielding is 1 for solid lines and 10 for dashed lines. (a) Remote shear strain $\gamma^\infty = 0.1\gamma_Y$, where $\gamma_Y = \sqrt{3}\sigma_Y/E$ is the yield strain in pure shear; (b) remote shear strain $\gamma^\infty = \gamma_Y$.

times the yield stress σ_Y. It is observed that the curves corresponding to $\beta = 1$ and $\beta = 10$ are quite separate near the interface, but begin to converge away from the interface, indicating a clear boundary layer effect. For a much larger remote loading $\gamma^\infty = \gamma_Y$, shown in Fig. 9(b), the boundary layer effect becomes much more significant; that is, the curves converge much more slowly. This model problem clearly shows that, even though the mesoscale cell size has little effect on global physical quantities such as bending moment, torque, and remotely applied stress, it can affect the local deformation and strain fields, particularly near a solid interface. In other words, the parameter β may be important to the local deformation field.

6.2. The axisymmetric fiber-matrix interaction in shear

In order to further investigate the role of mesoscale cell size on the local deformation field, we examine a fiber embedded in an infinite matrix subjected to shear parallel to the fiber direction. This is similar to a fiber pull-out problem, looking at the behavior away from the fiber ends and neglecting the fiber/matrix interfacial debonding. A cylindrical rigid fiber of radius a is bonded to an infinite matrix material. The cylindrical coordinates (r, θ, x_3) are set such that the x_3 axis coincides with the fiber axis. The matrix material is subjected to remote shear in the x_3 direction.

The only non-vanishing displacement is $u_3 = w(r)$, which depends only on r due to axisymmetry. The non-vanishing strains and strain gradients in cylindrical coordinates are

$$\epsilon_{r3} = \epsilon_{3r} = \frac{1}{2}\frac{dw}{dr}, \quad \eta_{rr3} = \frac{d^2w}{dr^2}, \quad \eta_{\theta\theta3} = \frac{1}{r}\frac{dw}{dr}.$$

The effective strain ϵ and effective strain gradient η are given by

$$\epsilon = \frac{1}{\sqrt{3}}\frac{dw}{dr}, \quad \eta = \frac{1}{2}\sqrt{\left(\frac{d^2w}{dr^2}\right)^2 + \left(\frac{1}{r}\frac{dw}{dr}\right)^2}.$$

The constitutive Eqs. (19) and (20) give non-vanishing deviatoric stresses and higher-order stresses as

$$\sigma'_{r3} = \sigma'_{3r} = \frac{1}{\sqrt{3}}\sigma, \tag{72}$$

$$\tau'_{rr3} = \frac{l_\epsilon^2}{36}\frac{\sigma_Y^2 f(\epsilon)f'(\epsilon)}{\sigma}\frac{d^2w}{dr^2},$$

$$\tau'_{\theta\theta3} = \frac{l_\epsilon^2}{36}\frac{\sigma}{\epsilon}\frac{1}{r}\frac{dw}{dr},$$

$$\tau'_{3rr} = \tau'_{r3r} = \frac{l_\epsilon^2}{288}\left[\frac{3\sigma_Y^2 f(\epsilon)f'(\epsilon)}{\sigma}\frac{\mathrm{d}^2 w}{\mathrm{d}r^2} - \frac{\sigma}{\epsilon}\frac{1}{r}\frac{\mathrm{d}w}{\mathrm{d}r}\right],$$

$$\tau'_{3\theta\theta} = \tau'_{\theta3\theta} = -\frac{l_\epsilon^2}{288}\left[\frac{\sigma_Y^2 f(\epsilon)f'(\epsilon)}{\sigma}\frac{\mathrm{d}^2 w}{\mathrm{d}r^2} - \frac{3\sigma}{\epsilon}\frac{1}{r}\frac{\mathrm{d}w}{\mathrm{d}r}\right],$$

$$\tau'_{333} = -\frac{l_\epsilon^2}{144}\left[\frac{\sigma_Y^2 f(\epsilon)f'(\epsilon)}{\sigma}\frac{\mathrm{d}^2 w}{\mathrm{d}r^2} + \frac{\sigma}{\epsilon}\frac{1}{r}\frac{\mathrm{d}w}{\mathrm{d}r}\right]; \tag{73}$$

where σ is the flow stress given in (16), and l_ϵ is the mesoscale cell size in (23).

The hydrostatic stress H is zero, and the equilibrium Eq. (6) becomes

$$r\sigma'_{r3} - \tau'_{rr3} + \tau'_{\theta\theta3} - r\frac{\mathrm{d}\tau'_{rr3}}{\mathrm{d}r} = A, \tag{74}$$

where A is a constant representing the amplitude of remotely applied shear stress because σ'_{r3} is on the order of Ar^{-1} as $r \to \infty$. The other remote boundary condition is the vanishing of the higher-order stress traction, i.e. $\tau'_{rr3}(r \to \infty) = 0$. Since the matrix is bonded to a rigid fiber, the displacement and rotation must vanish at the interface, so that

$$w = \frac{\mathrm{d}w}{\mathrm{d}r} = 0 \quad \text{at} \quad r = a. \tag{75}$$

It should be pointed out that the strain gradient effects come not only from the higher-order boundary conditions at the fiber/matrix interface, but also from the intrinsic characteristics of non-uniform deformation in this example. Even if the higher-order boundary condition $\mathrm{d}w/\mathrm{d}r = 0$ is not imposed at the interface, classical plasticity still gives a non-uniform distribution of shear stress $\sigma_{r3} = A/r$, where r is the polar radius in the cylindrical coordinates, and A is the same constant as in (74) for the amplitude of remotely applied shear stress. Therefore, this example illustrates combined effects of higher-order boundary conditions as well as the intrinsic strain gradients in the higher order theory.

The displacement, normalized by the corresponding value at a distance of 20% of fiber radius to the fiber/matrix interface (i.e. at $r = b = 1.2a$), vs the normalized distance to the interface, r/a, is shown in Fig. 10. The void radius a is the same as the intrinsic material length l. The Young's modulus E is 500 times the yield stress σ_Y. The curve for $\beta = 10$ is much higher than that for $\beta = 1$, indicating a strong dependence of the local deformation field on the mesoscale cell size. This confirms the conclusion established in section 6.1 that, even though the mesoscale cell size has little effect on global physical quantities such as the remotely applied stresses, it can affect the local deformation and strain fields.
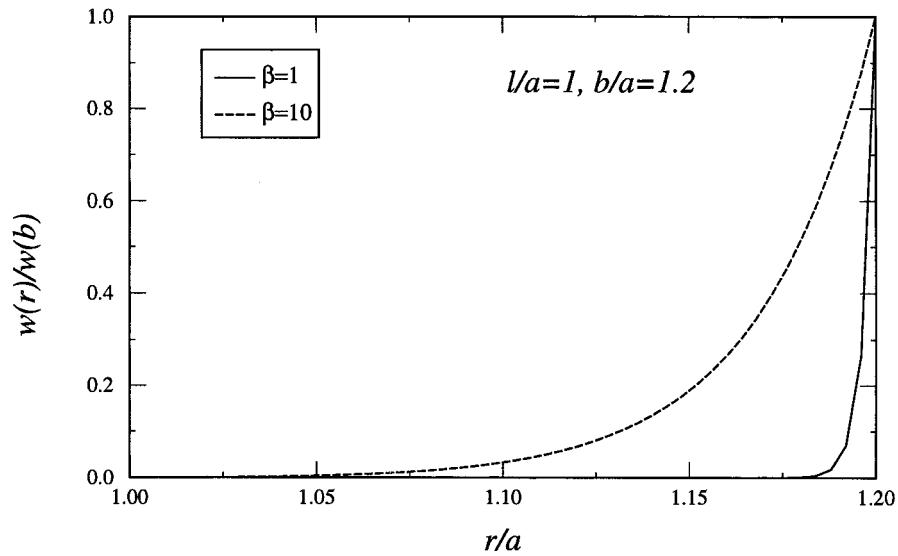
Fig. 10. The displacement, normalized by the corresponding value at a distance of 20% of fiber radius to the fiber/matrix interface (i.e. at $r = 1.2a$), vs the normalized distance to the interface, r/a. The void radius a is the same as the intrinsic material length l. Plastic work hardening exponent $N = 0.2$, Young's modulus $E = 500\sigma_Y$, shear modulus $\mu = 200\sigma_Y$, the coefficient α for Taylor's dislocation model $= 0.4$, and the ratio β of mesoscale cell size l_ϵ to dislocation spacing at plastic yielding is 1 for solid lines and 10 for dashed lines.

7. Summary

In this paper, we have used the mechanism-based strain gradient (MSG) plasticity to investigate several sample applications, including bending of thin beams, torsion of thin wires, growth of microvoids, cavitation instabilities, and bimaterials in shear. It is established that, in general, results based on MSG plasticity are quite different from those of classical plasticity theories, particularly when the characteristic length of the deformation is on the order of microns or smaller. It is established that the mesoscale cell size l_ϵ has little effect on the global physical quantities such as bending moments, torques, and applied stresses, though it can affect the local deformation field, particularly near the boundary of a solid. Results of this study are summarized in the following.

1. In bending of thin beams or torsion of thin wires, strain gradients significantly increase the plastic work hardening of materials, particularly when the beam thickness or wire radius is on the order of microns. For the same curvature in bending (or twist per unit length in torsion), the bending moment (torque) for micron-sized beams (wires) can be three times that estimated from classical plasticity. At small curvatures, however, MSG plasticity seems to underestimate the bending moment reported by Stolken and Evans (1998), and gives a smaller bending moment (or torque in torsion) than phenomenological strain gradient

plasticity does (Fleck and Hutchinson, 1993, 1997; Fleck et al., 1994). However, this comparison between MSG plasticity and phenomenological strain gradient plasticity gives an opposite trend when the curvature (twist per unit length) becomes large.

2. Although strain gradients delay void growth and cavitation instabilities to larger mean stresses, this effect is only significant for submicron-sized voids. For micron-sized voids, the increase in resistance against void growth and cavitation instabilities is only a few percent over that of classical plasticity. This is consistent with the estimate by phenomenological strain gradient plasticity (Fleck and Hutchinson, 1997). However, for submicron-sized voids, strain gradient effects are important. For example, a void size of 0.5 μ in copper can give a 40% increase in cavitation stress in MSG plasticity, while the increase is even higher (more than 100%) in phenomenological strain gradient plasticity.

3. The mesoscale cell size introduced in the multiscale framework in Part I of this study (Gao et al., 1999) has little effect on the global physical quantities such as bending moments, torques, and applied stresses. But it can change the local deformation field significantly, as observed near interfaces in bimaterials.

Acknowledgements

References

Begley, M.R., Hutchinson, J.W., 1998. The mechanics of size-dependent indentation. J. Mech. Phys. Solids 46, 2049–2068.

Bishop, R.F., Hill, R., Mott, N.F., 1945. The theory of indentation and hardness tests. Proc. Phys. Soc. 57, 147–159.

Fleck, N.A., Hutchinson, J.W., 1993. A phenomenological theory for strain gradient effects in plasticity. J. Mech. Phys. Solids 41, 1825–1857.

Fleck, N.A., Hutchinson, J.W., 1997. Strain gradient plasticity. Advances in Applied Mechanics 33, 295–361.

Fleck, N.A., Muller, G.M., Ashby, M.F., Hutchinson, J.W., 1994. Strain gradient plasticity: theory and experiment. Acta Metallurgica et Materialia 42, 475–487.

Gao, H., Huang, Y., Nix, W.D., Hutchinson, J.W., 1999. Mechanism-based strain gradient plasticity— I. Theory. J. Mech. Phys. Solids 47, 1239–1263.

Gurson, A.L., 1977. Continuum theory of ductile rupture by void nucleation and growth: part I–yield criteria and flow rules for porous ductile media. J. Eng. Mater. Technol. 99, 2–15.

Huang, Y., 1991. Accurate dilatation rate for spherical voids in triaxial stress fields. J. Appl. Mech. 58, 1084–1086.

Huang, Y., Hutchinson, J.W., Tvergaard, V., 1991. Cavitation instabilities in elastic-plastic solids. J. Mech. Phys. Solids 39, 223–241.

Koiter, W.T., 1964. Couple stresses in the theory of elasticity, I and II. Proc. K. Ned. Akad. Wet. (B) 67, 17–44.

Mindlin, R.D., 1964. Micro-structure in linear elasticity. Arch. Ration. Mech. Anal. 16, 51–78.

Mindlin, R.D., 1965. Second gradient of strain and surface tension in linear elasticity. Int. J. Solids Struct. 1, 417–438.

Needleman, A., Tvergaard, V., Hutchinson, J.W., 1992. Void growth in plastic solids. In: Argon, A.S. (Ed.), Topics in Fracture and Fatigue. Springer-Verlag, New York, pp. 145–178.

Nix, W.D., Gao, H., 1998. Indentation size effects in crystalline materials: a law for strain gradient plasticity. J. Mech. Phys. Solids 46, 411–425.

Rice, J.R., Tracy, D.M., 1969. On the ductile enlargement of holes in triaxial stress fields. J. Mech. Phys. Solids 17, 201–217.

Stolken, J.S., Evans, A.G., 1998. A microbend test method for measuring the plasticity length scale. Acta Materialia 46, 5109–5115.

Tvergaard, V., 1990. Material failure by void growth to coalescence. Adv. Appl. Mech. 27, 83–147.

Toupin, R.A., 1962. Elastic materials with couple stresses. Arch. Ration. Mech. Anal. 11, 385–414.